

Article

Spinodal Decomposition in Natural Bornite–Chalcopyrite Intergrowths: A Way of Cu-(Fe)-Sulfide Mineral Growth

Rui Liu ¹, Lei Zuo ¹, Peng Zhang ¹, Dongping Tao ^{1,*}, Huaizhi Shao ^{1,*}, Gang Tao ² and Kun Wang ³¹ School of Resources and Environmental Engineering, Shandong University of Technology, Zibo 255000, China² School of Environment and Resource, Southwest University of Science and Technology, Mianyang 621010, China³ School of Resources and Geosciences, China University of Mining and Technology, Xuzhou 221116, China

* Correspondence: authors: dptao@sdut.edu.cn (D.T.); shaohuaizhicumt@outlook.com (H.S.)

Abstract: Spinodal decomposition is an important mechanism of exsolution. However, spinodal decomposition has not been observed in natural sulfide intergrowths. We utilized focused ion beam (FIB) and transmission electron microscopy (TEM) techniques to confirm spinodal decomposition in natural sulfide intergrowths (chalcopyrite and bornite). According to FIB and TEM analyses, spinodal decomposition occurred as small and curving alternating dark and bright fluctuations in natural bornite–chalcopyrite intergrowths. Due to the low temperature that drove the exsolution mechanism, fluctuations ~10 nm wide and 20–200 nm long contained non-stoichiometric and tetragonal bornite and chalcopyrite. The corresponding electron diffraction of spinodal decomposition displayed a satellite spot in the $[-210]$ direction for bornite, and the $(200)^*$ and $(224)^*$ of chalcopyrite paralleled the $(24-2)^*$ and $(242)^*$ of bornite, respectively. These observations all agreed with spinodal decomposition, two coexisting phases formed with a crystallographic orientation relationship, which indicated the first observation of spinodal decomposition in natural sulfide intergrowths. These findings confirmed that spinodal decomposition is a mechanism for natural crystal growth. As spinodal decomposition is larger in extent and faster than nucleation and growth, other Cu ore deposits may also form via this mechanism.

Keywords: spinodal decomposition; exsolution; FIB-TEM; crystal growth

Citation: Liu, R.; Zuo, L.; Zhang, P.; Tao, D.; Shao, H.; Tao, G.; Wang, K. Spinodal Decomposition in Natural Bornite–Chalcopyrite Intergrowths: A Way of Cu-(Fe)-Sulfide Mineral Growth. *Minerals* **2022**, *12*, 1636. <https://doi.org/10.3390/min12121636>

Academic Editor: Thomas N. Kerestedjian

Received: 31 October 2022
Accepted: 17 December 2022
Published: 19 December 2022

Publisher's Note: MDPI stays neutral with regard to jurisdictional claims in published maps and institutional affiliations.



Copyright: © 2022 by the authors. Licensee MDPI, Basel, Switzerland. This article is an open access article distributed under the terms and conditions of the Creative Commons Attribution (CC BY) license (<https://creativecommons.org/licenses/by/4.0/>).

1. Introduction

The formation of many minerals involves exsolution. If a solution phase, which is chemically homogeneous at high temperature, becomes a polyphase equilibrium (by cooling, for instance), it may be viewed as unmixed. Two different mechanisms of exsolution were first introduced by Gibbs [1] and verified by subsequent mineralogical research [2–4]. During nucleation and growth, compositional fluctuations are large in degree but small in extent, while in spinodal decomposition, the compositional fluctuations are small in degree but large in extent [5]. The latter serves as the kinetic pathway for exsolution when the originally homogeneous phase is unstable relative to small compositional fluctuations. Spinodal decomposition occurs by interdiffusion of chemical constituents, without nucleation barriers or spontaneously growing compositional fluctuations, and it occurs faster than nucleation and growth. Therefore, spinodal decomposition readily occurs in rapidly cooled rocks and cases where nucleation kinetics are sluggish. The two phases decomposed by spinodal decomposition always maintain a coherent relationship, and the two phases only differ in chemical composition; the crystal structure is the same [5]. Therefore, the two phases formed by spinodal decomposition have a coherent lattice and a crystallographic orientation relationship. Thus, the two phases formed by spinodal decomposition can show satellite spots of electron diffraction. In addition, the stress and strain generated during spinodal decomposition are relatively small, and the coherent relationship is not

easily destroyed. However, in order to reduce the coherent strain energy, spinodal decomposition always grows along the crystal direction with the lowest coherent strain energy, resulting in a certain periodic pattern in its structure, such as alternating dark and bright fluctuations [5].

Spinodal decomposition is well-known, and exsolution has been reported often in rapidly cooled minerals [2]. For examples, Champness and Lorimer [6] found that minerals can form during the mechanism of spinodal decomposition. Piers et al. [7] revealed spinodal decomposition in a titanomagnetite examined by transmission electron microscopy. Weinbruch and Wolfgang [8] reported spinodal decomposition occurring in clinopyroxene and plagioclase, and Golla-Schindler et al. [2] directly observed spinodal decomposition in a magnetite–hercynite system. However, spinodal decomposition has not been reported in natural sulfide intergrowths, although this phenomenon has been demonstrated in bulk alloys and minerals using theoretical, computational, and experimental techniques [9]. In addition, the occurrence of sinusoidal compositional fluctuations formed during spinodal decomposition has not yet been found by microanalytical techniques [8].

Chalcopyrite (CuFeS_2 , cp) and bornite (Cu_5FeS_4 , bn) are the most abundant primary Cu-bearing sulfides across a wide range of mineral deposit types, both of which are members of the same broad sulfide structural family with cubic or tetragonal structures based on the formation temperature [10]. In nature, the majority of chalcopyrite and bornite intergrowths, such as bornite intergrown with a maze of minute chalcopyrite needles, have been interpreted in terms of solid-state exsolution or unmixing processes [11,12]. Therefore, chalcopyrite and bornite intergrowths serve as representative samples to study exsolution mechanisms.

The focused ion beam (FIB) and transmission electron microscopy (TEM) methods are now well established [13–15] and are powerful petrographic tools for the analyses of silicate minerals [16–18]. In addition, they are also applied to sulfide minerals (such as in Deditius et al. (2011) [19], Liu et al. (2021) [20], and so on). FIB and TEM examine the textures, compositions, and structures at any location of a sample on the sub-nanometer (atomic) scale [21]. As spinodal decomposition occurs on the nanoscale level, FIB and TEM excel in studying this phenomenon in chalcopyrite and bornite intergrowths.

In this contribution, we report the use of FIB cross-section imaging and use TEM to observe spinodal decomposition that occurred in natural chalcopyrite and bornite solutions. Selected area electron diffraction (SAED) and energy-dispersive X-ray spectrometry (EDS) confirmed the lattice parameters and the metal compositions. We confirm a new exsolution mechanism of natural sulfide minerals.

2. Materials and Methods

2.1. Samples

Natural chalcopyrite and bornite intergrowths samples were collected from the 109 porphyry copper ore deposit located in the western Awulale metallogenic belt in north-western China. The samples were polished and observed by optical microscopy. The chemical compositions of the micro-chalcopyrite and -bornite solid solutions ($\sim\mu\text{m}$) were investigated using an electron microprobe analyzer (EMPA). Having selected an area, the dual beam instrument used an ion beam to cut a slice and prepare site-specific specimens for TEM study.

2.2. Analytical Methods

2.2.1. EMPA

Major and trace elemental compositions of the chalcopyrite and bornite solutions were obtained by electron microprobe analysis (EMPA, JEOL JXA-8230) at the Key Laboratory of Mineralogy and Metallogeny of the Chinese Academy of Sciences. Peak calibrations for each element were conducted using reference materials, a beam current of 20 nA, an acceleration voltage of 20 kV, and a 1 μm spot size. Chalcopyrite and bornite were measured for Cu, S, Fe, Ag, Au, As, Co, and Ni with the peak counting time scaled from 10 to 60 s

and reduced by half for background counting depending on the element. The following mineral and synthetic metal standards were used: FeS₂ (Fe, S), Cu (Cu), FeAsS (As), Au (Au), Ag (Ag), Co (Co), and Ni (Ni).

2.2.2. FIB and TEM

TEM was used complementarily to obtain highly magnified images and structural/chemical information of both the sulfide matrix and the contained mineral nanoparticles. In situ determination of morphologies and crystal structures was conducted using selected area electron diffraction (SAED) of high-resolution images, and the major elemental distribution was qualitatively determined by energy-dispersive X-ray spectrometry (EDS). Cross-section images and TEM samples were prepared on an FEI-Helios NanoLab dual focused ion beam and scanning electron microscope (FIB-SEM) (FEI Talos F200X, Thermo Fisher Scientific, Waltham, MA, USA). After milling the samples with Au, the TEM foils, attached to Cu grids via Pt welding, were extracted and then thinned to 50–70 nm. Images were taken in immersion mode to maximize resolution.

The selected samples were observed using an FEI Tecnai G2 F20 TEM operated at 200 kV, equipped with an EDS detector (~0.5–1 wt.% detection limit), at the Sinoma New Materials Research Institute (Guangzhou, China) Co., Ltd. High-angle annular dark-field scanning transmission electron microscope (HAADF-STEM) imaging was performed using an ultra-high-resolution and probe-corrected FEI Titan Themis STEM. Probe correction delivered sub-Angstrom spatial resolution, and an inner collection angle greater than 50 mrad was used for HAADF experiments using a Fischione HAADF detector.

3. Results

3.1. Composition of Bornite–Chalcopyrite Intergrowths

In bornite–chalcopyrite intergrowths, bornite has a distinct “amaranth” color, and submicron lamellar sets of chalcopyrite are commonly “yellow” (Figure 1a), as shown by reflected light under natural light. Chalcopyrite and bornite in solution primarily contain Fe, Cu, and S (Table 1). However, they are both non-stoichiometric, i.e., the ratios of (Cu + Fe)/S (<1.5) and Cu/Fe (<5) of bornite are lower than the ideal bornite composition (Cu₅FeS₄), and the ratios of (Cu + Fe)/S (>1) and Cu/Fe (>1) of chalcopyrite are higher than the ideal composition of chalcopyrite (CuFeS₂, Table 1).

Table 1. EMPA data of sulfides in the 109 Cu deposit (impurities total less than 3%).

Samples	S (wt.%)	Cu (wt.%)	Fe (wt.%)	(Cu+Fe)/S	Cu/Fe
chalcopyrite	34.66	37.31	28.26	1.00	1.14
	32.33	38.00	26.89	1.05	1.22
	32.17	38.64	26.27	1.06	1.27
	31.54	39.72	25.74	1.09	1.33
	32.88	41.21	25.32	1.06	1.40
	32.52	40.81	24.96	1.06	1.41
	32.61	43.37	24.63	1.09	1.52
bornite	26.17	62.80	11.41	1.43	4.74
	26.09	61.82	11.18	1.41	4.76
	24.98	63.80	11.29	1.52	4.87
	25.02	62.93	11.48	1.50	4.72
	25.76	61.00	11.02	1.41	4.77
	26.33	62.51	11.25	1.41	4.79
	26.47	62.16	11.35	1.40	4.72
	26.08	62.92	11.49	1.44	4.72
25.93	62.03	10.97	1.42	4.87	

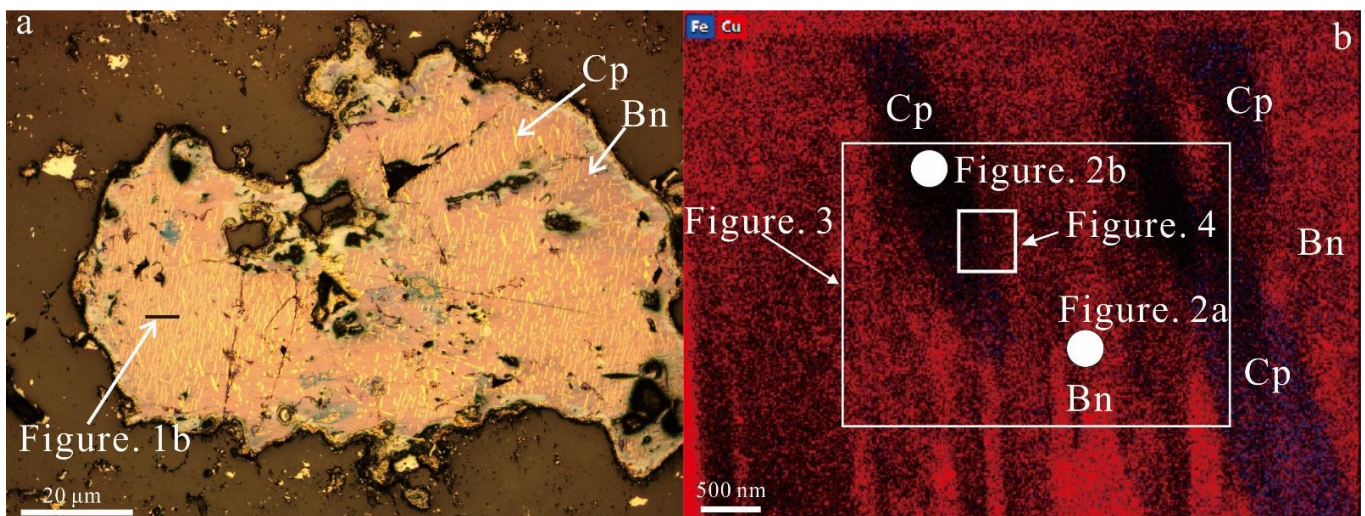


Figure 1. (a) Exsolution texture of Cu-(Fe)-sulfides from the 109 Cu deposit, showing the submicron yellow lamellar sets of chalcopyrite exsolution in the “amaranth” bornite. The black label is the location for FIB; (b) EDS mapping for FIB cross-section imaging of bornite–chalcopyrite intergrowths, showing that a set of sub-micrometer-sized lamellae of chalcopyrite in bornite are parallel with one another. Cp: chalcopyrite, Bn: bornite. The white square is the location of HR-TEM of the bornite–chalcopyrite intergrowths. The white circles are the locations of EDS spot analysis.

3.2. Nanoscale (FIB and TEM) Characterization of Bornite–Chalcopyrite Intergrowths

To ensure that the small-scale samples of bornite–chalcopyrite intergrowths included chalcopyrite and bornite, we cut a slice through the chalcopyrite and bornite as show in Figure 1a. The slice was excavated from the mineral surface to the interior, forming a $4\ \mu\text{m} \times 5\ \mu\text{m}$ slice (Figure 1b). In this slice, chalcopyrite appeared relatively blue to dark in the EDS mapping (Figure 1b), and bornite appeared relatively red in the EDS mapping (Figure 1b) were intergrowth. The compositions of chalcopyrite and bornite were also confirmed by TEM-EDS (Figure 2). The chalcopyrite lamellae were thinner (1–2 nm) and shorter, mainly growing along two orientations. In addition, the sub-micrometer-sized lamellae of chalcopyrite were parallel to one another (Figure 1b), which is consistent with the characteristics of chalcopyrite at larger scales (Figure 1a). In addition, there are numerous small, alternating dark and bright fluctuations, ~ 10 nm wide and 20–200 nm long, occurring in the HR-TEM image of bornite–chalcopyrite intergrowths (Figure 3). In the enlarged HR-TEM image, one growing orientation of chalcopyrite is $(200)_{\text{Cp}}^*$, which runs parallel to $(24-2)_{\text{Bn}}$, and the other is $(224)_{\text{Cp}}^*$, which runs parallel to $(242)_{\text{Bn}}^*$ (Figure 4). SAED of the high-resolution image in Figure 5 shows that there are numerous satellite spots of electron diffraction occurring along the $[-210]$ direction for bornite (Figure 5).

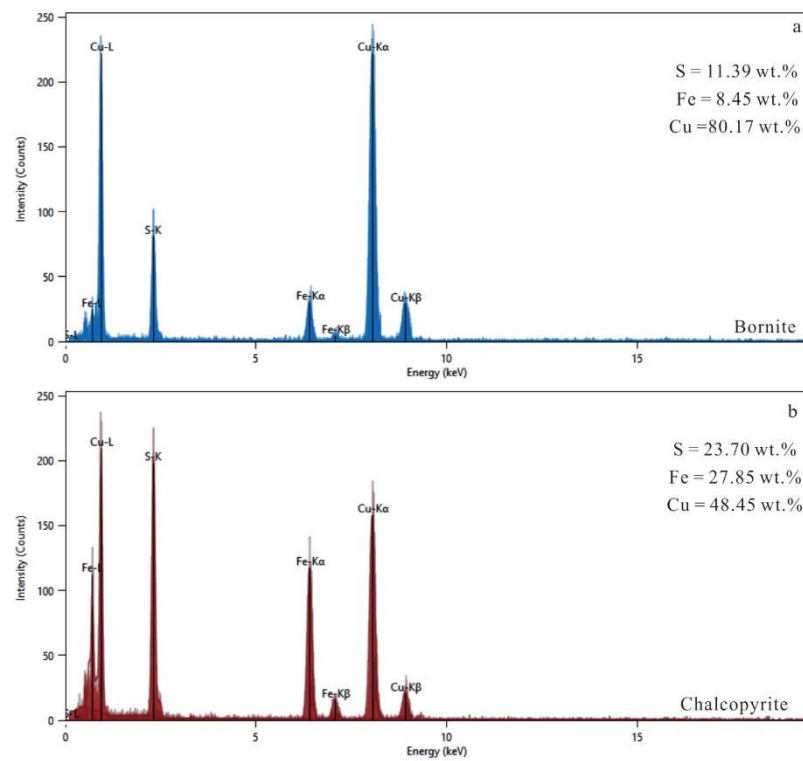


Figure 2. (a) TEM-EDS spectra for bornite; (b) TEM-EDS spectra for chalcopyrite.

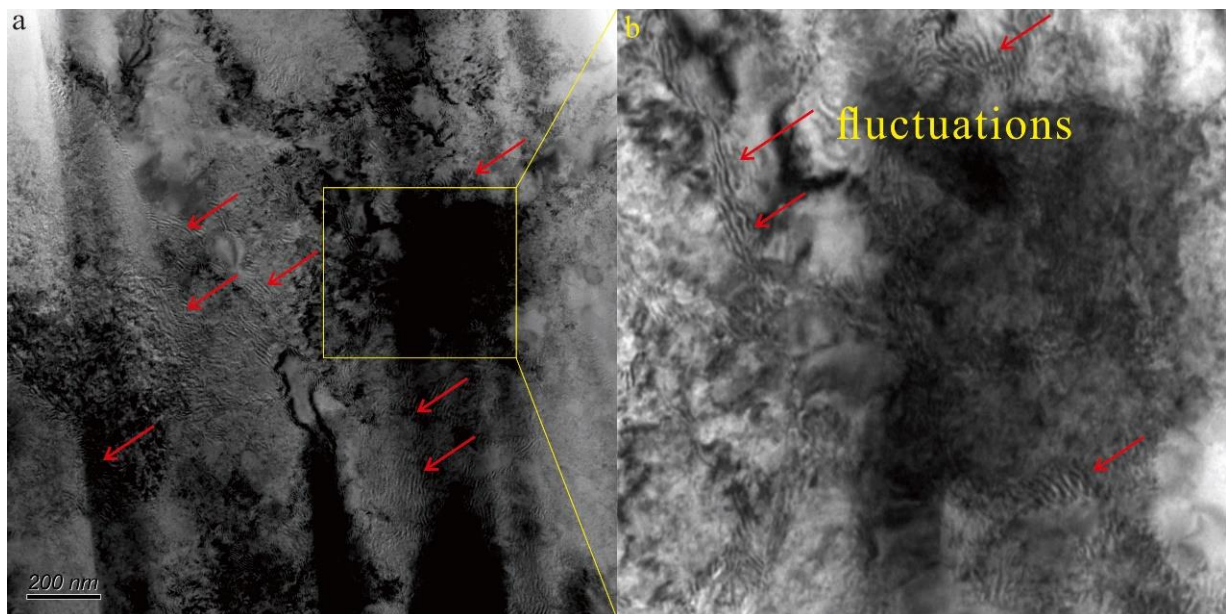


Figure 3. (a) HR-TEM imaging of the bornite–chalcopyrite intergrowths, showing that many small alternately dark and bright fluctuations occur in the chalcopyrite and bornite solid solutions (red arrow). (b) High-magnification transmission electron microscopy image obtained from the yellow square in Figure 3a.

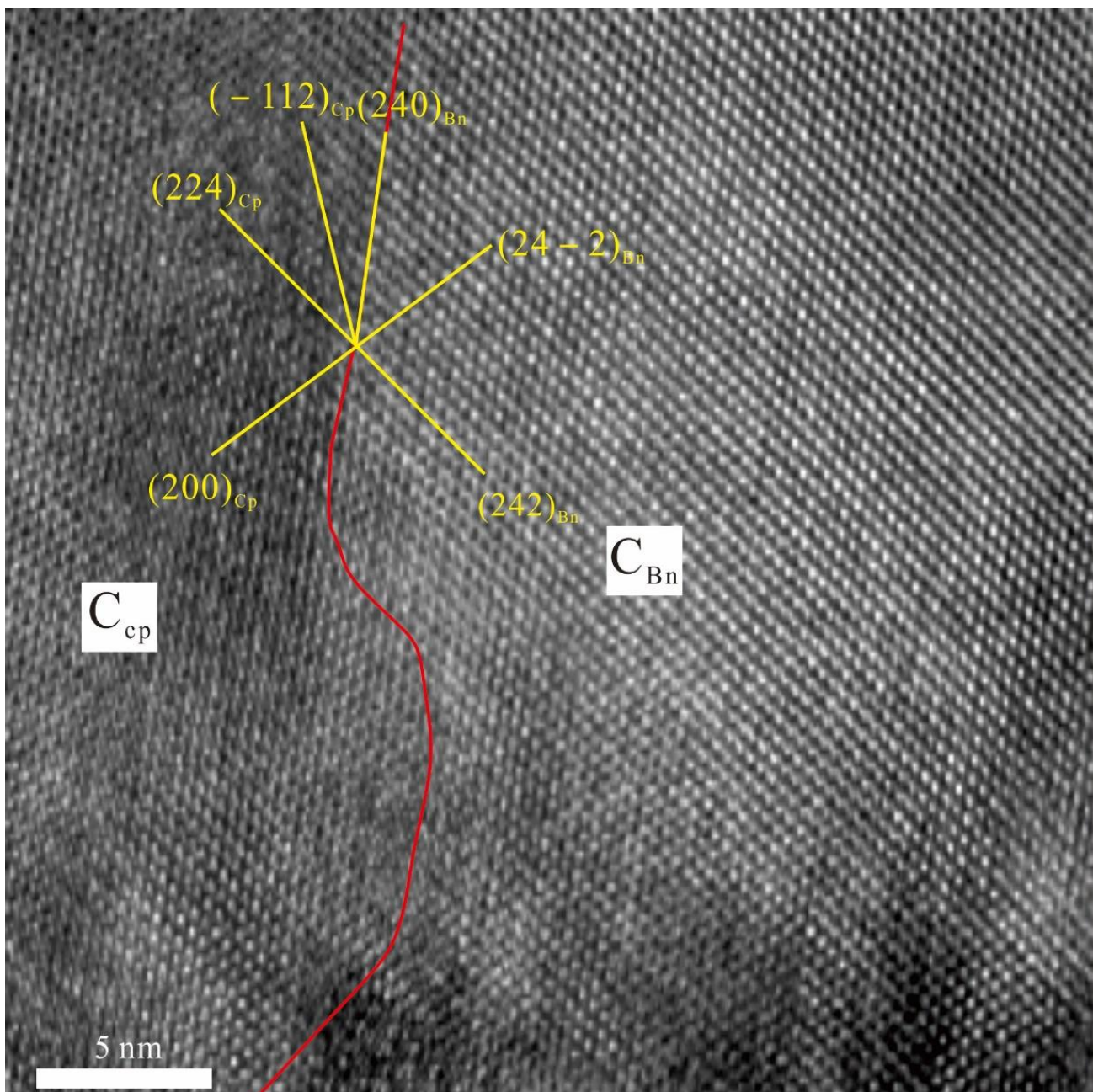


Figure 4. Enlarged HR-TEM imaging of the bornite–chalcopyrite intergrowths, showing that the $(200)^*$ and $(224)^*$ of chalcopyrite paralleled the $(24-2)^*$ and $(242)^*$ of bornite, respectively. The red line is the boundary of chalcopyrite and bornite.

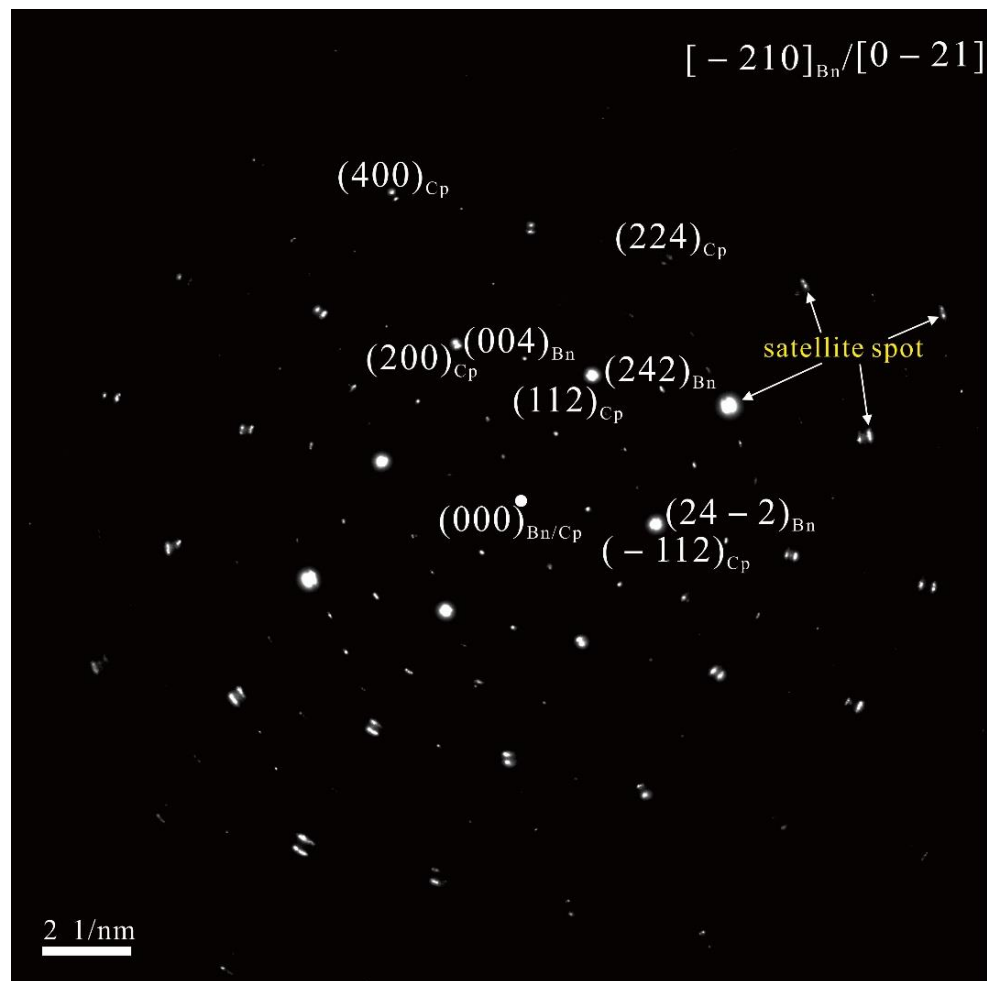


Figure 5. The electron diffraction of spinodal decomposition, showing satellite spots along the $[-210]$ direction for bornite.

4. Discussion

4.1. Genesis of the Bornite–Chalcopyrite Intergrowths

According to the EMPA results, both chalcopyrite and bornite occur in non-stoichiometric ratios, indicating that chalcopyrite–bornite assemblages with a tetragonal crystal structure form at a lower temperature (<228 °C) [10]. As the chalcopyrite-forming exsolutions drove the formation mechanism [22], the $(\text{Cu} + \text{Fe})/\text{S}$ and Cu/Fe ratios for bornite were lower, but they were higher for chalcopyrite. In addition, deviation from these values is considered non-stoichiometric due to the cooling of higher-temperature bornites [22]. In the FIB cross-section imaging (Figure 1b), chalcopyrite displays intergrowth with bornite, and chalcopyrite forms in the bornite interior, which indicated that chalcopyrite formed via exsolution [22]. Overall, we confirmed two mineral phases, chalcopyrite and bornite, occurred in the exsolution texture, and the chalcopyrite–bornite assemblages were the primary mineral, not the secondary replacement.

4.2. Spinodal Decomposition in Natural Bornite–Chalcopyrite Intergrowths

Previous studies have proven that minerals formed by spinodal decomposition always has a certain periodic pattern in their structures which has the lowest coherent strain energy [2]. In this study, TEM imaging revealed many small, alternating dark and bright fluctuations in the bornite–chalcopyrite intergrowths (Figure 3), which is consistent with the periodic pattern. In addition, these fluctuations all curve, which indicates that they formed via spinodal decomposition [23]. In addition, due to the strain energy being lowest in a coherent lattice, the two phases formed by spinodal decomposition have a coherent

lattice and a crystallographic orientation relationship. Therefore, the two phases always show satellite spots of electron diffraction. The satellite spots of electron diffraction along the $[-210]$ direction for bornite (Figure 5) in this study also demonstrated the occurrence of spinodal decomposition. Although a Moiré fringe, which is a periodicity fringe formed by the superposition of two identical atomic layers, can also form the satellite spot of electron diffraction, it usually appears as a straight stripe and obviously differs from the fluctuations occurring in our samples. In addition, a Moiré fringe forms via the movement of two lamellae with identical compositions which are continuous and cover a wide scope (\sim micrometer scale). Therefore, lamellae forming a Moiré fringe are usually $n \times 10^3$ nm in size, large enough that the contrast is obvious. However, in our samples, we observed neither large lamellae ($>n \times 10^3$ nm) nor an obvious contrast. Instead, we found many small lamellae and two mineral phases with different compositions. Therefore, these fluctuations likely occurred in bornite–chalcopyrite intergrowths formed by spinodal decomposition.

In addition, as two coexisting phases formed by spinodal decomposition have a crystallographic orientation relationship, they should share parallel crystal faces. HR-TEM images of the bornite–chalcopyrite intergrowths showed the $(200)^*$ and $(224)^*$ of chalcopyrite were parallel to the $(24-2)^*$ and $(242)^*$ of bornite (Figure 4), respectively, which agrees with formation via spinodal decomposition. As spinodal decomposition is one mechanism of exsolution [5], crystal structures of two coexisting phases formed by spinodal decomposition are similar, e.g., magnetite and hercynite [2], pigeonite and diopside [24], and tetragonal $Zr_{1-c}Y_cO_{2-c/2}$ and cubic $Zr_{1-c}Y_cO_{2-c/2}$ [4]. Chalcopyrite and bornite formed at lower temperatures were both tetragonal, which agrees with spinodal decomposition. Therefore, we concluded that spinodal decomposition occurred in natural bornite–chalcopyrite intergrowths.

4.3. Implication of Spinodal Decomposition in Mineralogy

Spinodal decomposition is an important mechanism of exsolution [2] whose study has theoretical significance and practical applications. In materials science, alloys formed through spinodal decomposition may have greater strength and toughness, e.g., Zr-Nb alloys [25] and Cu-Ni-Cr alloys [26]. Almost all permanent magnetic alloys form via spinodal decomposition [27]. In earth science, many natural minerals form solid solutions, e.g., the pigeonite/diopside exsolution in the Allende granular olivine pyroxene [28] and the hematite/ilmenite exsolution in the Panxi region [29]. However, the mechanisms of natural mineral exsolution were thought to occur through nucleation and growth [30]. This work provides strong evidence that natural minerals can also form via spinodal decomposition. Our findings indicate that elemental segregation in natural solutions not only occurs as downhill diffusion but also as uphill or negative diffusion. This mechanism for mineral formation is larger in extent and faster than nucleation and growth. Therefore, it is important for natural mineral formation.

5. Conclusions

FIB and TEM revealed spinodal decomposition in natural bornite–chalcopyrite intergrowths via high-resolution examination of textures, compositions, and structures at specific locations on a sample in unprecedented detail. Many small, alternating dark and bright fluctuations occurred in natural bornite–chalcopyrite intergrowths. Furthermore, the data showed satellite spots of electron diffraction and two coexisting phases with similar crystallographic orientations and different compositions. This new mechanism of mineral growth may have important significance for natural minerals formed in the Earth.

Author Contributions: Methodology, L.Z. and G.T.; formal analysis, P.Z. and K.W.; D.T., investigation; H.S., data curation; R.L., writing—review and editing; R.L., funding acquisition. All authors have read and agreed to the published version of the manuscript.

Funding: This research was funded by National Natural Science Foundation of China (Grant No. 42102076) and Science Foundation of Shandong Province (ZR2021QD037).

Data Availability Statement: Not applicable.

Acknowledgments: We are grateful to numerous technical staff members for their assistance in this study. Comments and suggestions from the journal's anonymous reviewers greatly improved the quality of this work.

Conflicts of Interest: The authors declare no conflict of interest.

References

1. Gibbs, J.W. *Scientific Papers*; Dover: New York, NY, USA, 1961; pp. 105–252.
2. Golla-Schindler, U.; O'Neill, H.S.C.; Putnis, A. Direct observation of spinodal decomposition in the magnetite-hercynite system by susceptibility measurements and transmission electron microscopy. *Am. Mineral.* **2005**, *90*, 1278–1283. [[CrossRef](#)]
3. Abart, R.; Petrishcheva, E.; Wirth, R.; Rhede, D. Exsolution by spinodal decomposition II: Perthite formation during slow cooling of anatectites from Ngorongoro, Tanzania. *Am. J. Sci.* **2009**, *309*, 450–475. [[CrossRef](#)]
4. Rudraraju, S.; Anton, V.D.V.; Garikipati, K. Mechanochemical spinodal decomposition: A phenomenological theory of phase transformations in multi-component, crystalline solids. *NPJ Comput. Mater.* **2016**, *2*, 16012. [[CrossRef](#)]
5. Qi, Z.F. *Diffusion and Phase Transformation in Solid Metals*; Machinery Industry Press: New York, NY, USA, 1998; pp. 349–357.
6. Champness, P.E.; Lorimer, G.W. Exsolution in silicates. In *Electron Microscopy in Mineralogy*; Wenk, H.-R., Ed.; Springer: Berlin, Germany, 1975; pp. 174–204.
7. Piers, P.K.S. Spinodal decomposition in a titanomagnetite. *Am. Mineral.* **1980**, *65*, 1038–1043.
8. Weinbruch, S.; Wolfgang, F.M. Exsolution and coarsening in ironfree clinopyroxene during isothermal annealing. *Geochim. et Cosmochim. Acta* **2003**, *67*, 5071–5082. [[CrossRef](#)]
9. Ramanarayan, H.; Abinandanan, T.A. Spinodal decomposition in polycrystalline alloys. *Phys. A* **2003**, *318*, 213–219. [[CrossRef](#)]
10. Amcoff, Ö. Experimental replacement of chalcopyrite by bornite: Textural and chemical changes during a solid-state process. *Miner. Depos.* **1988**, *23*, 286–292. [[CrossRef](#)]
11. Cook, N.J.; Ciobanu, C.L.; Danyushevsky, L.V.; Gilbert, S. Minor elements in bornite and associated Cu-(Fe)-sulfides: A LA-ICP-MS study. *Geochim. Et Cosmochim. Acta* **2011**, *73*, 4761–4791. [[CrossRef](#)]
12. Ramdohr, P. *The Ore Minerals and Their Intergrowths*; Elsevier: Amsterdam, The Netherlands, 2013; pp. 1–1174.
13. Lee, M.R. Transmission electron microscopy (TEM) of Earth and planetary minerals: A review. *Mineral. Mag.* **2010**, *74*, 1–27. [[CrossRef](#)]
14. Liu, R.; Bo, B.Y.; Tao, D.P.; Chen, G.W. Bastnäsite nanoparticles in carbonatite-syenite-hosted REE deposit: Implication for La and Ce migration and bastnäsite growth. *Chemosphere* **2021**, *271*, 129831. [[CrossRef](#)]
15. Zuo, Y.S.; Gao, Z.X.; Zuo, L.; Zhang, P.; Liu, R.; Zhang, Q.; Zhang, T.T. Ultrastructure of a columbite-tantalite mineral from the Zhaojinggou Ta-Nb deposit in the North China Craton: Direct evidence of the formation mechanism of the columbite-group minerals. *Geofluids* **2022**, *2022*, 8125419. [[CrossRef](#)]
16. Lee, M.R.; Brown, D.J.; Smith, C.L.; Hodson, M.E.; MacKenzie, M.; Hellmann, R. Characterization of mineral surfaces using FIB and TEM: A case study of naturally weathered alkali feldspars. *Am. Mineral.* **2007**, *92*, 1383–1394. [[CrossRef](#)]
17. Deditius, A.P.; Utsunomiya, S.; Reich, M.; Kesler, S.E.; Ewing, R.C.; Hough, R.; Walshe, J. Trace metal nanoparticles in pyrite. *Ore Geol. Rev.* **2011**, *42*, 32–46. [[CrossRef](#)]
18. Liu, X.; Liu, R.; Chen, G.W.; Luo, X.E.; Lu, M.Q. Natural HgS nanoparticles in sulfide minerals from the Hetai goldfield. *Environ. Chem. Lett.* **2020**, *18*, 941–947. [[CrossRef](#)]
19. Liu, R.; Cao, J.J.; Hu, G. Revealing a new transport form of natural material by naturally occurring spherical amorphous silica particles in soil aerosol. *Chem. Geol.* **2020**, *559*, 119950. [[CrossRef](#)]
20. Liu, R.; Lin, X.B.; Wang, G.Q.; Liu, X. Natural N-bearing nanoparticles in sediments of a shallow bay of the south China: A new N form in N-cycling. *Ecol. Indic.* **2021**, *122*, 107281. [[CrossRef](#)]
21. Ciobanu, C.L.; Cook, N.J.; Utsunomiya, S.; Pring, A.; Green, L. Focussed ion beam–transmission electron microscopy applications in ore mineralogy: Bridging micro- and nanoscale observations. *Ore Geol. Rev.* **2011**, *42*, 6–31. [[CrossRef](#)]
22. Ciobanu, C.L.; Cook, N.J.; Ehrig, K. Ore minerals down to the nanoscale: Cu-(Fe)-sulphides from the iron oxide copper gold deposit at Olympic Dam, South Australia. *Ore Geol. Rev.* **2017**, *81*, 1218–1235. [[CrossRef](#)]
23. Lecoq, N.; Zapolsky, H.; Galenko, P. Evolution of the structure factor in a hyperbolic model of spinodal decomposition. *Eur. Phys. J. Spec. Top.* **2009**, *177*, 165–175. [[CrossRef](#)]
24. Weinbruch, S.; Wolfgang, F.M. Constraints on the cooling rates of chondrules from the microstructure of clinopyroxene and plagioclase. *Geochim. Et Cosmochim. Acta* **1995**, *59*, 3221–3230. [[CrossRef](#)]
25. Guo, C.P.; Zi, J.L.; Li, C.R.; Du, Z.M. Spinodal Decomposition Microstructure in Zr-Nb Alloys. *Chin. J. Rare Met.* **2017**, *41*, 672–677, (in Chinese with English abstract).
26. Chou, A.; Datta, A.; Meier, G.H.; Soffa, W.A. Microstructural behaviour and mechanical hardening in a Cu-Ni-Cr alloy. *J. Mater. Sci.* **1978**, *13*, 541–552. [[CrossRef](#)]
27. Rong, C.L.; Liu, N.; Zhang, X.B.; Zhou, J.; Lu, M.H. Review on the Spinodal Decomposition in Hard Materials. *Cem. Carbide* **2006**, *23*, 42–46.

28. Carpenter, M.A. A “conditional spinodal” within the peristerite miscibility gap of plagioclase feldspars. *Am. Mineral.* **1981**, *66*, 553–560.
29. Tan, W.; Wang, C.Y.; He, H.P.; Xing, C.M.; Liang, X.L.; Dong, H. Magnetite-rutile symplectite derived from ilmenite-hematite solid solution in the xinjie Fe-Ti oxide-bearing, mafic-ultramafic layered intrusion (SW China). *Am. Mineral.* **2015**, *100*, 2348–2351. [[CrossRef](#)]
30. Cacciuto, A.; Auer, S.; Frenkel, D. Onset of heterogeneous crystal nucleation in colloidal suspensions. *Nature* **2004**, *428*, 404–406. [[CrossRef](#)]